Available online at www.sciencedirect.com
SCIENCE DIRECT®
International Journal of Heat and Mass Transfer 48 (2005) 4887–4903
International Journal of HEAT and MASS TRANSFER
www.elsevier.com/locate/ijhmt

# Flow and heat transfer of confined impingement jets cooling using a 3-D transient liquid crystal scheme

Ting Wang [a,*], Mingjie Lin [b], Ronald S. Bunker [c]

[a] Energy Conversion and Conservation Center, University of New Orleans, New Orleans, LA 70148-2220, USA
[b] Department of Mechanical Engineering, Clemson University, Clemson, SC 29634-0921, USA
[c] General Electric Corporate R&D, Schenectady, NY 12301, USA

Received 3 May 2004; received in revised form 15 April 2005
Available online 15 July 2005

**Abstract**

It has been shown that the heat transfer coefficients obtained from using the 1-D transient liquid crystal scheme are higher than those obtained from employing the 3-D scheme when surface heat transfer is highly nonuniform such as on a hot surface subject to jet impingement cooling. This is due to the fact that 1-D method does not include the lateral heat flows induced by local temperature gradients. The objective of this study is to provide a new database of heat transfer coefficient distribution on the jet impingement target surface in the confined cavity by employing a 3-D transient liquid crystal scheme. The study is performed with an $8 \times 11$ array of confined impinging jets with Reynolds numbers ranging from 1039 to 5175. The 1-D results are higher than the 3-D results with the local maximum and minimum heat transfer values being overvalued by about 15–20% and the overall heat transfer by approximately 12%. In addition, hot-film measurements of the flow structure are conducted to gain insight into the effects of cross-flow on heat transfer behavior. The surface mapping of heat transfer coefficient demonstrates a change from columnar pattern to a horizontal pattern and switching back to the columnar pattern as Reynolds number increased consecutively. This pattern switching is thought to be caused by the competition between jet penetration and the cross-flow buffering effect. A non-uniformity index is defined to provide a quantitative measure for cooling effectiveness for various cases. The results indicate that increased cross-flow degrades the heat transfer performance but increase uniformity.


*Keywords:* Inverse transient scheme; Transient liquid crystal scheme; Impingement jets

## 1. Introduction

Jet impingement cooling or drying is one of the widely employed heating or cooling methods in many practical applications. Some examples are annealing of metal and glass, electrical equipment cooling, and drying of paper and textiles or other thin films as well as in the secondary cooling of continuous casting of steels. There are many different ways of employing jet impingement cooling such as using single jets, pulsed jets, inclined jets, 2-D slot jets, array of discrete jets, and annular jets. In gas turbines, jet impingement has been commonly employed for cooling combustion liners, transition pieces, and airfoils. For gas turbine components to survive under increasingly raised higher temperature environment

* Corresponding author. Tel.: +1 504 280 7183; fax: +1 504 280 5539.
*E-mail address:* twang@uno.edu (T. Wang).

0017-9310/$ - see front matter © 2005 Elsevier Ltd. All rights reserved.
doi:10.1016/j.ijheatmasstransfer.2005.04.020

**Nomenclature**

| | |
|---|---|
| $c_p$ | specific heat |
| $D$ | jet diameter |
| $H$ | overall average value of heat transfer coefficient of the entire surface |
| $H_Z$ | spanwise average heat transfer coefficient for each column |
| $h$ | convective heat transfer coefficient (W/m$^2$ °C) |
| $k$ | heat conductivity |
| $L$ | length of the test surface |
| $m$, $n$ | total number of heat transfer measurement locations (or pixel) in $z$- and $x$-directions |
| $Nu_{cx}$ | Nusselt number in the absence of cross-flow |
| $Nu_x$ | Nusselt number $\equiv hD/k$ |
| $q''$ | heat flux |
| $Re$ | $V_j d/v$ |
| $S$ | internal generation source term |
| $t$ | time |
| $T$ | temperature |
| $T_{u,v}$ | turbulence intensity based on $u', v' \equiv \frac{\sqrt{(u'^2+v'^2)/2}}{V_{tot}}$ |
| TLC | transient liquid crystal scheme |
| $U$, $V$ | mean velocity components in $x$-and $y$-directions |
| $V_j$ | jet velocity |
| $u'$, $v'$ | RMS velocity fluctuation components |
| $x$ | streamwise direction, parallel to the target surface |
| $y$ | jet impingement direction, normal to the target surface |
| $Y$ | impingement target distance |
| $z$ | spanwise direction (see Fig. 1) |
| $\rho$ | density |
| $\sigma$ | a nonuniformity index of $h$, defined as the standard deviation of $h$ |
| $\sigma_Z$ | spanwise average of $\sigma$ |
| $\overline{\sigma_z}$ | normalized $\sigma_Z \equiv \sigma_Z/H_z$ |

*Subscripts*

| | |
|---|---|
| $i$, $j$ | indices of the locations |
| $w$ | wall |

to improve thermal efficiency, jet impingement cooling will continue to be a critical technique for cooling gas turbine hot components.

Research results during the past four decades on jet impingement heat transfer are available in a large body of the literature. Livingood and Hrycak [1], Martin [2], Downs and James [3], Humber and Viskanta [4], and Jambunathan et al. [5], for example, have provided extensive reviews of the literature.

One specific feature for gas turbine component cooling is that the jet flows are confined in a narrow space. The major player that affects jet impingement cooling in a confined space is the cross-flow (or spent flow). Cross-flow is defined as the flow moving in the direction normal to the impingement flow. Cross-flow prevails in situations employing multiple arrays of jets, including the impingement jets cooling situations in the gas turbine vanes, blades, and combustion liners. For confined impingement arrays, the interactions between cross-flow (or spent flow) and adjacent jets can further deteriorate the heat transfer performance of downstream jets. According to the producing source, most cross-flow can be categorized as two types: imposed cross-flow and spent jet flow. The imposed cross-flow results from the external flow resource; whereas the spent cross-flow is induced by the accumulated spent flow moving toward the exit.

For the imposed cross-flow case, Huang et al. [6] conducted a numerical investigation on the effect of the cross-flow rate on the heat transfer performance under a turbulent impinging slot jet. They compared the predicted Nusselt number distribution including the effect of cross-flow with those without cross-flow. It was found that the location of the maximum Nusselt number shifted downstream due to the deflection of the jet by the cross-flow. They further observed that the Nusselt number far downstream from the slot exit for the case with imposed cross-flow was higher than that without cross-flow, which was in agreement with the Metzger et al.'s [7] experimental observation on round jets in an imposed cross-flow. The increase of the Nusselt number over the downstream region was due to the total mass flow rate exhausted through downstream direction that increased as the cross-flow rate was increased.

In most practical cases, the cross-flow encountered is resulted from accumulating spent flow along the main flow direction. Obviously, considering the complex interaction between the cross-flow and the impingement flow, it is expected that the cross-flow will have significant impact on both the flow structure and the heat transfer characteristics. It is logical to assume that the flow field under the first few rows of impingement holes should be subjected to less cross-flow effect than that of downstream holes. Spent air from the upstream jets in an array normally lowers heat transfer coefficients, and to the limit the cross-flow can sweep away the jets so that impingement is prevented. Therefore, it is antici-

pated that the heat transfer should continuously diminish in the downstream area.

For example, Galant and Martinez [8] reported that the heat transfer near the stagnation point from an array of jets was lowered 7% from a single jet value due to interactions of adjacent jets and spent flow from upstream. Such interference results in the formation of unpredictable variations of local heat transfer between jets including offset of local cooling peaks near stagnation points. They presented a formulation of the cross-flow influence upon impingement heat transfer rates for arrays of circular jets: $Nu_x = (Nu_{cx} + Nu_x)\Psi$, where $Nu_{cx}$ is the Nusselt number in the absence of cross-flow and $Nu_x$ and $\Psi$ are analytical functions of $Z/D$ (impingement distance to jet diameter ratio), $m$ (cross-flow to jet momentum ratio), and $Re$ (cross-flow Reynolds number based on jet spacing).

Goldstein and Timmers [9] showed that spent air from upstream jets tended to lower local heat transfer coefficients and, in the limit, a flow visualization showed that the cross-flow can sweep away the downstream jets such that the jet impingement was prevented. A series of studies of jet impingements heat transfer including the effect of cross-flow were conducted by Florschutz et al. [10–12]. Florschuetz [13] found that increasing the ratio between the imposed cross-flow mass flow rate and impingement jet flow rate from 0.2 to 0.4 could significantly reduce Nusselt number by a factor greater than 2.5.

Bruchez and Goldstein [14] experimentally studied the influence of cross-flow on the heat transfer characteristic of partially confined and staggered impinging jets issuing from discrete round holes and slots respectively. For single or multiple jets, flow visualization results showed that the cross-flow made the flow highly three-dimensional, which also increased the complexity of the flow structure and heat transfer situation. The experimental results showed that heat transfer was lowered due to the interaction of adjacent jets and the induced boundary layer separation and corresponding flow eddies. Also, such interaction resulted in the formation of the secondary heat transfer peaks between jets. Goldstein and Timmers [9] illustrated the similar heat transfer phenomena resulting from the cross-flow effects through isotherms obtained by flow visualization techniques.

Recently, Huang et al. [15] presented detailed heat transfer distributions for an array of in-line jets impinging on a plate with different crossflow orientations by employing a transient liquid crystal method. The different crossflow directions were created by changing the test section open ends. They reported that the highest heat transfer coefficients are obtained for a crossflow orientation where flow exits in both directions.

Almost all the data in gas turbine applications are in the range with Reynolds number higher than 5000. Low Reynolds number data ($Re < 5000$) are needed for applications in some areas of combustor guided vanes, combustor transition pieces, and nozzle endwalls. Especially for alternate materials such as ceramic matrix composites (CMC) or continuous fiber ceramic composites (CFCC) or monolithic ceramics. For such new materials, the operating stress that they can withstand is much lower than for metals, yet they can take higher bulk temperatures. This combination of conditions can lead to the use of lower internal cooling effectiveness in order to reduce the thermal gradients through the wall, and so keep the thermal stresses within the material limitations. This is an important class of application that will become more common in the coming years.

Although jet impingement cooling has the advantage of achieving significantly enhanced overall heat transfer rates, it inherently suffers from a highly nonuniformed cooling distribution between the jets. The conventional measuring schemes including using discrete thermocouples and employing 1-D transient liquid crystal (TLC) are subject to some limitations due to highly nonuniformed surface cooling. Discrete thermocouples are difficult to effectively catch the detail of local nonuniform cooling distribution, and the 1-D TLC scheme does not include the lateral heat flows induced by local temperature gradients, which are pronounced under jet impingement cooling conditions. These limitations motivate this study to employ a 3-D TLC scheme to obtain more accurate surface heat transfer coefficient distribution under highly nonuniform impingement jet cooling conditions. In addition, information of flow structures is indispensable for improving understanding of convective heat transfer. However, information of simultaneous measurements of flow structure with corresponding surface heat transfer coefficient measurements is still lacking in confined space conditions. Therefore, this study will also employ hot-wire measurements of flow structure within the confined space.

In summary, the reasons that motivate this study are:

1. Lack of data for low-Reynolds number (<5000) confined jet impingement cooling to serve increasing needs in some of gas turbine applications.
2. Inaccuracy of employing 1-D TLC scheme under highly nonuniform surface cooling conditions.
3. Lack of flow information to help interpret cross-flow effects on confined jet impingement heat transfer.

## 2. Experimental program

### 2.1. Flow circuit

The flow of the experiment was supplied by a dedicated compressor. To minimize the fluctuation of the compressor output, a 60-liter tank was installed at the outlet of the compressor. After the tank, the pipeline

was diverted into two branches: one led to the test section; the other one served as a by-pass. At the inlet of each branch of pipelines, a regulating valve was installed respectively. By adjusting these two valves, the flow rate through the test section could be conveniently controlled without disturbing the steady pressure level and the total flow rate. Before the inlet of the test section, a dryer and an oil filter were installed to remove moisture and any particles larger than 20 μm.

### 2.2. Test section

The test section, as shown in Fig. 1, had two chambers. Only the left chamber is used in this study. A thin (1.5 mm) aluminum plate with an array of in-line jet holes of 2 mm in diameter is placed in the left chamber. The inlet of each jet hole was slightly rounded to ensure similar entrance situation, whereas the outlet (facing the target surface) was square edged. The flow entered and exited the test section through three large holes of 2.54 cm (1 in.) in diameter. Flow from the compressor first came through the inlet and entered the left chamber, then flowed through the in-lined, uniformly distributed impingement holes on the aluminum plate and impinged on the first impingement target surface. The impingement spent air from the first stage further flowed into the right chamber. An $8 \times 11$ isothermal jet array was used with a jet-to-jet spacing of six diameters. The target distance was 12.7 mm (1/2 in.). The mass flow rate was measured at the flow exit by integrating the outlet velocity profile measured by a hot-film sensor.

### 2.3. Heated test surface

The heated test surface was designed to implement the transient liquid crystal method as shown in Fig. 1. The test surface consisted of five layers. The first layer was a clear LEXAN plate of 12.6 mm (1/2 in.) thick which served as the support for the heater and the liquid crystal sheet. The second layer was the liquid crystal

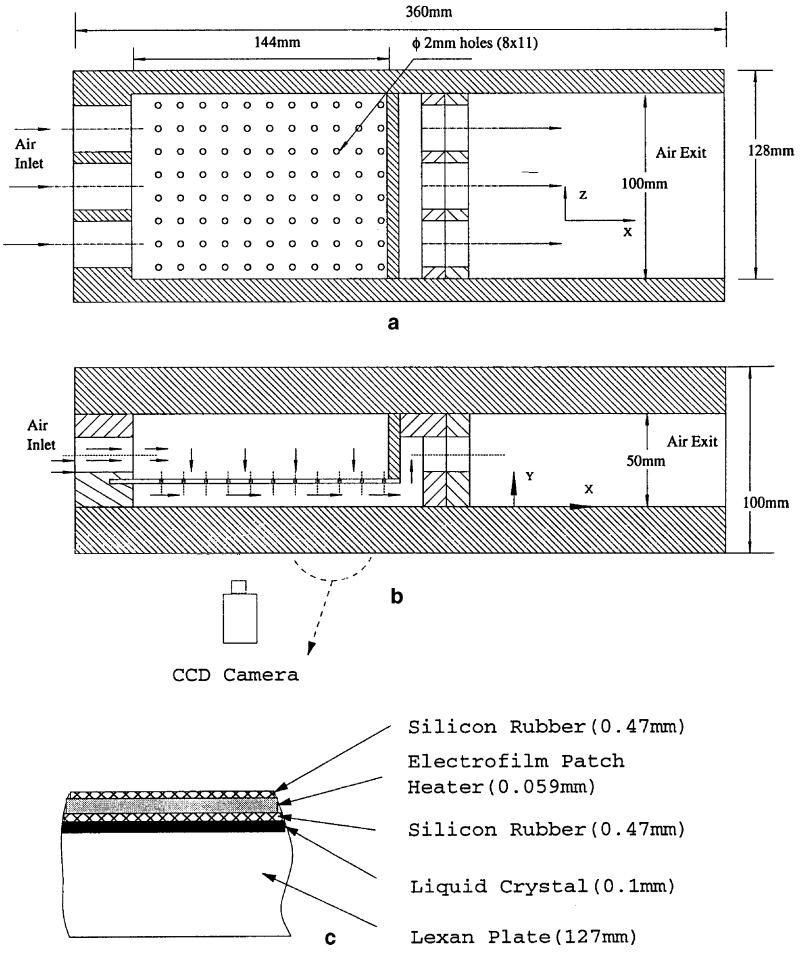


Fig. 1. Schematics of the test section and the composite heated wall: (a) front view, (b) top view, (c) cross-section of the heated wall.

sheet, which was about 0.1 mm thick with adhesive on both sides. The liquid crystal sheet (model number R30C5W, HALLCREST Inc.) had a temperature range of 30–35 °C. The third and fourth layer were the patch heater sandwiched between silicon rubber layer of 0.47 mm thick on both sides. The total thickness of the patch heater was approximately 1 mm and the actual thickness of etched heating foil was about 0.059 mm.

### 2.4. Thermocouples

Ten pairs of 40 gauge (0.003 in. in diameter) chromel–constantan thermocouples were deployed including 3 pairs embedded underneath the heater as the in situ calibration references for the liquid crystal, 2 pairs at the exit of the test section, 2 pairs for monitoring the ambient and inlet main flow temperatures, and 3 pairs on the backside of the test surface for detecting the heat losses, if any. The three embedded thermocouples are located in the centerline at $x = 12$, 87, and 162 mm, respectively. The tip of the thermocouple is approximately 0.008 in. (0.203 mm) in diameter. The area of each pixel is 0.208 mm × 0.213 mm. The size of the thermocouple tip is about the same size of the area represented by one pixel. The thermocouples were calibrated against an RTD in a circulating water bath.

### 2.5. 3-D inverse transient liquid crystal method

The transient liquid crystal method using 1-D heat conduction scheme has been widely employed for jet impingement heat transfer studies; for example, the measurements conducted by Van Treuren et al. [16] and Hwang and Cheng [17]. More complete procedures are employed in the three-temperature film cooling problem such as proposed by Vogel et al. [18], and Chambers et al. [19]. Theoretically, the following conditions need to be satisfied for employing the analytical 1-D transient solutions: (a) 1-D heat conduction, (b) imposing an instantaneous convective heating or cooling boundary condition on the surface, and (c) semi-infinite depth of the solid. Among these conditions, condition (a) is frequently violated by nearly all the applications. To satisfy conditions (b) and (c), inconvenient and/or complex designs are frequently required to be implemented. For example, in practical experiment cases, the ideal step temperature change on the test surface is not achievable. To deal with it, one must use a superimposed method to approximate the transient temperature changing curve on the test surface by integrating a finite number of step changes (see [20]). Depending on the time step size, the obtained data accuracy may not always be satisfying. Furthermore, for a situation like arrays of impingement jets cooling, a highly nonuniform distribution of heat transfer coefficient exists. 1-D method would introduce errors due to deviation from the one-dimensional assumption. To include the lateral heat conduction, this study employs the 3-D TLC scheme developed by Lin and Wang [21]. They applied a 3-D inverse transient conduction scheme in coupling with the transient liquid crystal method to back calculate the heat transfer distribution on the surface from the transient temperature reading of the test surface. Lin and Wang's scheme [21] is summarized below:

#### 2.5.1. Image processing system

First, a period of TLC color images on the test surface was recorded by a standard 8 mm camcorder. Then images were digitized to TIFF format. The image acquisition rate was set to be 30 images per second. The whole TLC color play history became a large number of discrete image TIFF files. Using Matlab image processing toolbox, each pixel of those images could be interpreted as a (R, G, B) data set. (R, G, B) represents the color intensity value of the three primary colors: red, green, and blue. The next step was to transform the color information in the RGB domain into the UVW domain. The linear transformation between the RGB system and the UVW system was through the matrix used by Hollingsworth et al. [22]. The hue angle was calculated at each pixel of the image after the three-dimensional RGB matrix was further transformed into a two-dimensional matrix UV [22]. For each pixel, the history of the hue angle change during the experiment was obtained. By looking through the hue angle's changing history, the time elapsed to reach a reference value (e.g., 32 °C) could be obtained at each pixel. At this stage, and for each case, the raw data had been reduced to a matrix $\tau(nx, ny)$, which stated the time period of each sampled pixel to reach the specific temperature level.

The next step of heat transfer data processing was to back calculate the heat transfer coefficient from the time elapse information. The 3-D inverse scheme was employed here. The temperature information obtained on the TLC surface was not on the true surface but a short distance beneath the surface. The unknown heat transfer coefficients were to be recovered as the boundary condition on the true surface of the heat conduction body. The dimensions and physical properties of the composite heated test surface and the heat flux generated by the heater were known. Using all these parameters as the input to the inverse scheme, the heat transfer coefficient at each location on the target surface could be calculated.

#### 2.5.2. 3-D inverse transient conduction scheme

For a transient heat conduction problem, the temperature distribution inside a solid can be found through numerical or analytical methods if the heat flux or temperature histories at the surface (i.e. the boundary conditions) of the solid are known. This is a direct problem. However, in many dynamic heat transfer situations, one of the boundary conditions, such as the surface heat

flux or surface heat transfer coefficient, are not known, and they must be determined from transient temperature measurements at interior locations. This kind of problem is categorized as the inverse problem. In the present study, the term "inverse" was used to emphasize the nature of the current problem in a broad sense. In this study, the known information was the time period to reach a specific temperature for each pixel over the TLC surface beneath the heater. The unknown to be solved was the heat transfer coefficient distribution on the test surface. A program written in Matlab was utilized to implement this scheme.

The inverse scheme consists of two stages. The first stage is to solve the direct heat conduction problem. The second stage is to correct the estimated heat transfer field. The heat transfer problem in this study is a 3-D transient heat conduction problem.

The transient conduction governing equation is $\rho c \frac{\partial T}{\partial t} = \nabla \cdot (k \nabla T) + S$. The numerical calculation was performed using the second order central differencing scheme for spatial axis and implicit method for temporal step. The discretization of the governing equation results in a large set of linear algebraic equations, which are solved by the Gauss–Seidel point-by-point iterative method. The results are deemed reaching convergence when the variation of consecutive results of at each grid point is than $10^{-6}$. After one round of solving a direct 3-D transient heat conduction problem, a predict-and-correct method is employed to adjust the input condition.

For this study, the inverse scheme starts with applying a guessed heat transfer coefficient distribution on the test surface as the boundary condition and compute the temperature field of the whole domain. The second step is to correct the previously guessed heat transfer coefficient distribution, and continue another run of 3-D transient heat transfer computation. This loop continues until the calculated transient temperature information (i.e. both time and temperature values) of each grid on the target surface matches the experimental data within the convergence criterion. During the correction process, the Newton root-finding method is adopted to correct the assumed heat transfer coefficient distribution.

The temperature of the back surface was set to the values read by two thermocouples on the back surface. In this study, since the Lexan substrate was selected to be thick enough as an insulator to reduce the back losses. The back surface temperature was able to be maintained at the ambient temperature during each experiment. On the other four surrounding sides of the test plate, adiabatic boundary condition was applied. The input information required for the calculation is: (1) the heat flux generated by the heater, (2) thermophysical properties of the materials including the test surface, heater and the composite substrate, (3) ambient temperature during the experiment, (4) the boundary conditions on all the boundaries including the guessed heat transfer coefficients on the front surface, (5) the initial condition of the entire computational domain, (6) the dimensions of the test surface, and (7) the grid system's configuration.

### 2.6. Experimental procedure

Before the experiments were conducted, the CCD camera was calibrated by using a standard color map to verify the digitization property and reliability of the particular camera used. A hardcopy of color map including the three primary colors was used as the reference. The CCD camera used for the heat transfer study was employed to record three images of the color map at different dates. The time interval between the taking of each image was 24 h. Those three images were then digitized by the image board and processed by the Matlab image toolbox. The RGB values of each pixel of these different images were compared and found to be consistently within 1.3%. It was concluded that the camera was reliable to use.

A pre-test of the color property of the liquid crystal sheet was conducted on the target surface heated with a constant heat flux without air impingement. The pre-test indicated that the foil heater delivered an acceptable uniformity of heating. The temperature variation between any two randomly chosen locations on the surface (or pixels of the TLC images) at any time during measurement was found within 0.2 °C with a $\Delta T$ $(=T_w - T_\infty)$ of 8 °C.

To minimize the deterioration of the color play properties of TLC sheet, the TLC surface was well covered and protected by a black card-board sheet and cloth immediately after each test. To eliminate errors due to lighting and viewing angle, an in situ calibration was performed for each experiment. In every test case, readings of three embedded thermocouples were used as the standard against which the color images were calibrated. The thermocouples themselves were calibrated against an RTD supplied and calibrated by NIST (National Institute of Standard and Technologies).

A heat transfer test was started about 20 min after the flow reached steady state by switching on the DC power supply of the heater. At the same time, the CCD camera and the thermocouple temperature measurement system were turned on. Three embedded thermocouple readings were matched by their physical (or real) time to produce the one-to-one relationship with the corresponding frame of the color image. By specifically looking at the hue angles of the TLC display at these three locations, a unique relationship between the temperature and the hue angle was established for each thermocouple location. Ideally, for one specific temperature, the hue angle derived from the temperature data of three locations should be identical. For the four

cases performed, the hue angle's variations were within 3%. The averaged calibration curve was used. The complete image change history during the transient tests was recorded by the CCD camera on an 8 mm tape, which acted as a raw data storage media. The response time of a 40-gauge thermocouple is approximately 0.1 s. The liquid crystal sheet's response time is about the same as the thermocouple. The transient period for sweeping through the color play region was approximately 4–7 min depending on the Reynolds number. The error induced between the thermocouple's and the liquid crystal's response time is negligibly small in comparison with the transient period and other uncertainty sources. Since the liquid crystal is calibrated in situ in the present study, the experimental setup, including lighting and camera, were not moved for different cases. The potential errors due to variations of illumination and camera viewing angle are removed.

In the present experimental situation, since the heat transfer condition was transient, the effect of development of thermal boundary layer needed to be evaluated. Several different heating processes using different amounts of heating power were performed under the same flow condition (or Reynolds number). The experimental results showed differences within 1%, which is believed including the effect of thermal boundary layer development but not exclusively.

### 2.7. Test section for flow measurement

During the flow experiments, the heated target surface was replaced with another LEXAN plate to allow for traversing the hot-film probe with minimal flow interference. To meet the measuring requirements and to minimize the disturbance of the introduction of the probes, slots and plugs of different sizes were made. Using a different combination of the plugs, measurements could be made at locations in the interested area with a 1.58 mm (1″/16) increment. Self-adhesive gaskets and vaseline were used to minimize air leakage to an unnoticeable level.

### 2.8. Flow measurements

In the beginning of each test, the flow system was allowed to warm up and reach steady state within 45 min. A standard commercial cross hot-film probe (TSI Model 1248A) was used in conjunction with the TSI IFA-100 hot-wire anemometers. An A/D data acquisition board Win-10DS/4 installed in a personal computer was employed for data acquisition and digitization. A software STREAMER was used to transfer data directly to the hard disk. The hot-film signals were sampled at 10 kHz for 20 s and were low-pass filtered at 5 kHz for each measurement. The hot-film probe was calibrated against a pitot tube connected to a micromanometer with a resolution of ±25.4 μm (±0.001 in.) of water.

The measurements were taken at 78 locations in the $x$-direction along the centerspan between the first and eighth jet columns. In the normal direction ($y$), the measurements were taken at two 2 locations, $y = 7.56$ mm (Plane I) and 3.78 mm (Plane II), respectively, as shown in Fig. 2.

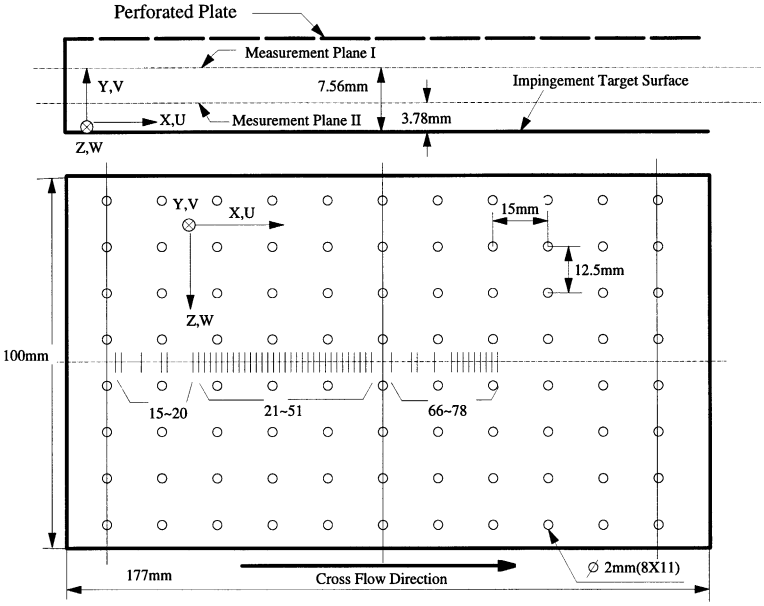


Fig. 2. Layout of hot-film measurement locations.

## 3. Uncertainty analysis

The uncertainty analysis was performed following the procedure proposed by Moffat [23]. The independent variables were traced and identified following the methodology proposed by Wang and Simon [24]. The overall $N$th order uncertainty for the heat transfer coefficient is 3.31% with the three largest uncertainties contributed by the main flow temperature, initial temperature, and test surface thickness. The detailed analysis was documented by Lin [25]. The uncertainty of hot film in high-turbulence flows is about 3% in mean velocity measurement and 15% in velocity fluctuation measurements.

## 4. Results and discussion

### 4.1. Heat transfer

The transient liquid crystal method has provided test results with decent spatial resolution for engineering needs. Each image frame consisted of $480 \times 752$ pixel data that covered an actual viewing area of 10 cm × 16 cm (height × length). Four experimental cases were conducted. The results of overall heat transfer coefficients are shown in Table 1. The first three experimental cases used the same confined impingement cavity with only the right side being open, but they differed in impingement jet Reynolds numbers. The fourth experimental case was conducted to investigate the effect of controlled cross-flow upon the heat transfer on the target surface by opening both ends of the impingement cavity, i.e. the hatched area at the lower left corner in Fig. 1(b) was completely opened by removing the LEXAN material; hence, part of the spent air exited on the left side.

### 4.2. Overall heat transfer

The overall results are shown in Table 1, in which $h_{min}$, $h_{max}$, and $H$ are defined as the minimum, the maximum and the overall average heat transfer coefficients, respectively. They are obtained from the entire target surface for each experimental case.

Table 1
The overall heat transfer results for four experimental cases

| Cases | 1 | 2 | 3 | 4 |
|---|---|---|---|---|
| $Re$ | 1039 | 3026 | 5133 | 5175 |
| $h_{min}$ (W/m$^2$ °C) | 11.80 | 48.61 | 50.78 | 102.2 |
| $h_{max}$ (W/m$^2$ °C) | 188.76 | 369.69 | 556.02 | 481.60 |
| $H$ (W/m$^2$ °C) | 71.91 | 203.92 | 355.82 | 323.10 |
| $H/Re$ (W/m$^2$ °C) | 0.0692 | 0.0674 | 0.0693 | 0.0624 |
| $Nu/Re$ | 0.00265 | 0.00258 | 0.00265 | 0.00239 |

The results indicate that the $h_{max}$ and $H$ increase linearly with the Reynolds number. The increasing rate of $H$ is about the same as the increasing rate of Reynolds number, while rate of increase of $h_{min}$ is a little slower than that of $h_{max}$. For the first three cases, the $H/Re$ values are within a constant value of $0.0682 \pm 1.4\%$ and the $Nu/Re$ values are $0.00265 \pm 1.4\%$ or $Nu = 0.00304\ Pr^{0.42}Re$. It seems that Cases 2 and 4 deviate from the linearity with Reynolds number. It will be shown later that this could be caused by the dominant cross-flow effect in Cases 2 and 4.

Case 3 has the highest $H$ of the four cases. This is obviously caused by the fact that Case 3 has the highest jet Reynolds number. Although Case 4 has a similar Reynolds number as Case 3, the heat transfer performance reduces. This phenomenon is believed to be due to the effect of cross-flow because Case 4 has two exits instead of one exit for Case 3.

The overall heat transfer coefficient results were compared with several previous studies as shown in Fig. 3. Kercher and Tabakoff [26] proposed $Nu/Pr^{1/3} = 0.00395Re^{0.966}$ for $4000 < Re < 40{,}000$. They investigated heat transfer of a square array of round air jets impinging perpendicularly to a flat surface including the effects of spent air, similar to the present study, but they used thermocouples to measure the temperature. The comparisons are also made with the correlation proposed by Huang [27]. Huang investigated the heat transfer coefficients for air flow through round jets impinging normal to a heat transfer surface. The present results agree well with Kercher and Tabakoff's correlations within 10% and fall between the correlations between [26,27]. Note that since this study conducted in a low Reynolds number region, the comparisons are

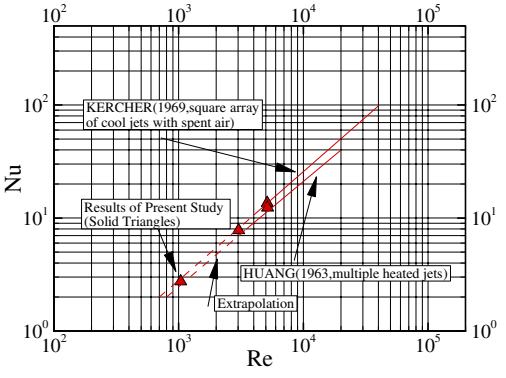


Fig. 3. Comparisons of the present experimental results with other studies. The dashed lines are extrapolations made by the present study.

made with the extrapolations of the correlations of [26,27].

In the following discussions, Cases 1, 2, and 3 are presented and discussed first. Case 4 will be separately discussed in the last section to focus on the effect of the controlled cross-flow on heat transfer.

### 4.3. Contour plots of the heat transfer coefficient distribution

The two-dimensional local $h$-distributions for Cases 1, 2, and 3 are presented in Fig. 4(a)–(c), respectively. Contour line plots are chosen to enhance the information

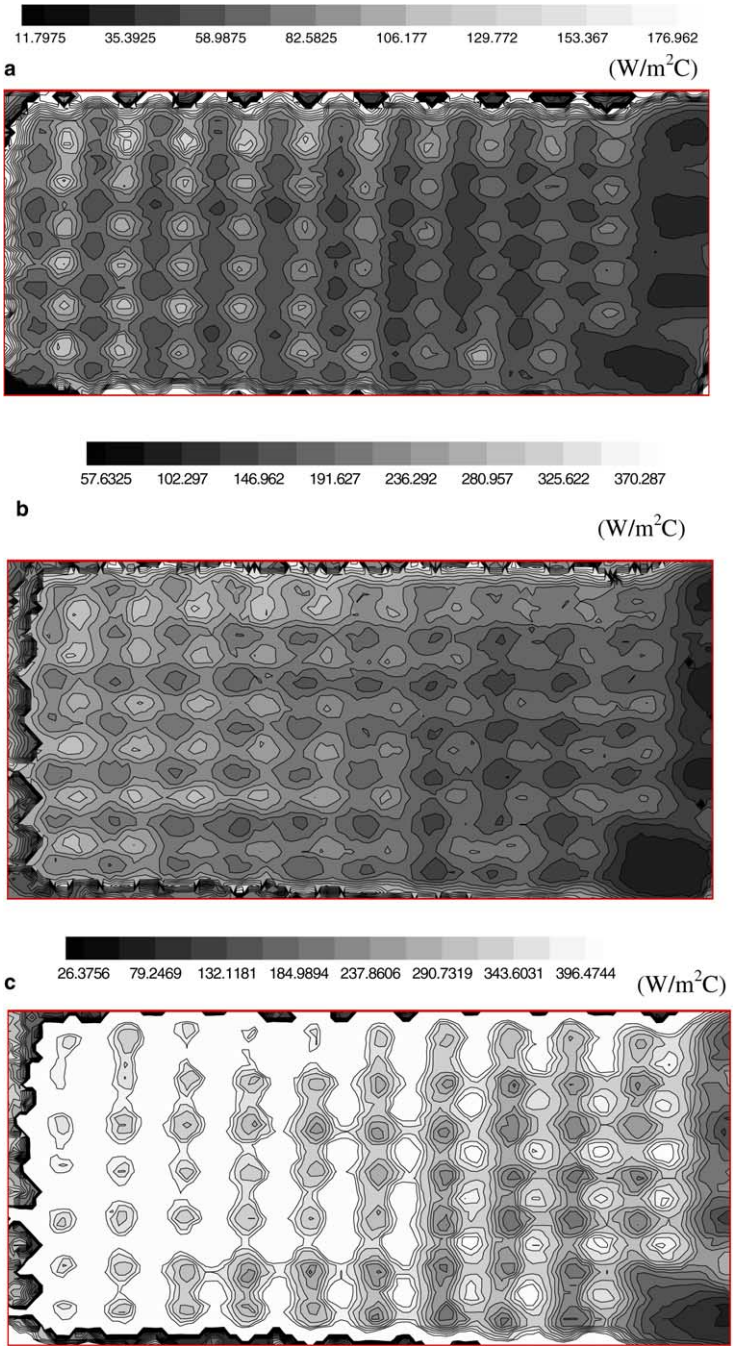


Fig. 4. Contour plot of convective heat transfer coefficient distribution on the impingement target surface: (a) Case 1 at $Re = 1039$ (b) Case 2 at $Re = 3026$, and (c) Case 3 at $Re = 5133$.

about the gradient of local $h$ variation. The contour lines are constant $h$ lines, and they are also representative of isotherms because $q'' = h(T_w - T_j)$, and at any snap shot, $q''$ and $T_j$ are nearly constant for each pixel. The interval value between each two successive contour level is a constant; therefore, the spacing between two lines or density of the contour lines per unit area demonstrates the magnitude of the local temperature gradient on the surface.

In Fig. 4, an array of light color spots can be identified as a strong heat transfer zone (or stagnation area) due to jet impingement cooling. The overall heat transfer performance of the upstream area (left portion) is noticeably better than that of the downstream area (right portion). The major portion of the surface shows a clear and consistent spanwise periodicity (in the $z$-direction), except near the edges of the target surface.

For Case 2 in Fig. 4(b), at first glance, the contour plot seems to have a similar heat transfer coefficient distribution pattern as Case 1, but they are different. Instead of being approximately round circles in a columnar pattern as in Case 1, the stagnation areas of Case 2 appear to be stretched in the $x$-direction and lose the columnar pattern. More horizontal lines have developed in the $x$-direction than in the vertical $z$-direction. Spacing between the contour lines in Case 2 are more uniform than Case 1. The change of contour line pattern from columnar pattern to horizontal pattern is thought to be associated with the cross-flow effect, which will be further discussed later.

The local heat transfer coefficient distribution of Case 3 is presented by Fig. 4(c). Again, higher heat transfer is associated with the upstream region. The overall magnitude of $h$ of Case 3 becomes higher, and, in contrast to Cases 1 and 2, contour lines become denser in the downstream region. The pattern of contour lines changes back to columnar pattern as in Case 1. In the stagnation regions of the first several columns of impingement jets, $h$ is higher and more uniform, which results in a larger blank area in the contour line plots.

To provide a more detailed and quantitative view of the $h$-distribution along the cross-flow direction, the value along a straight line through the centers of the fourth row of impingement holes is selected as a representative and is presented in Fig. 5. In all three cases, $h$ illustrates periodic variations; however, the periodic peak $h$-values do not exactly coincide with the location of the jet holes. This is believed to be caused by the sweeping effect of the cross-flow. $H$ variations tend to decline downstream except Case 2 in Fig. 5(b), which illustrates minor increase in the last two jets near the flow exit at the right-hand side of the figure. Different from Case 1, both Cases 2 and 3 exhibit low peak values near $x/L = 0$.

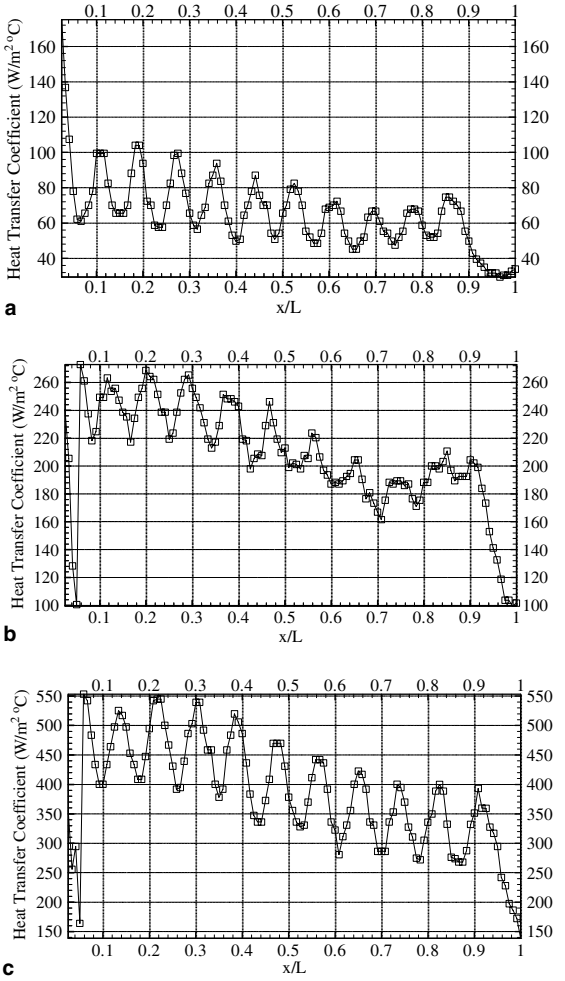


Fig. 5. Heat transfer coefficient distribution along a straight line in the $x$-direction through the centers of the fourth row of the jet holes: (a) Case 1 at $Re = 1039$, (b) Case 2 at $Re = 3026$, and (c) Case 3 at $Re = 5133$.

### 4.4. Spanwise average of heat transfer coefficients

To facilitate the analysis of the $h$-variation along the cross-flow direction, the whole target surface is divided into 88 sub-domains (8 rows × 11 columns) with the jet-hole location placed in the middle of each sub-domain. The measurement was made from a $240 \times 376$ array of pixels; therefore, each sub-domain contains $30 \times 34$ measurement points. The spanwise average heat transfer coefficient for each column is denoted as $H_Z$. Fig. 6 presents the results of spanwise average for each case. The maximum and minimum curves represent separately the spanwise averages of the peaks and valleys in each column, respectively. In Case 1 (Fig. 5(a)), the $H_Z$ value monotonically decreases toward the exit. This monotonic decrease of heat transfer coefficient has been

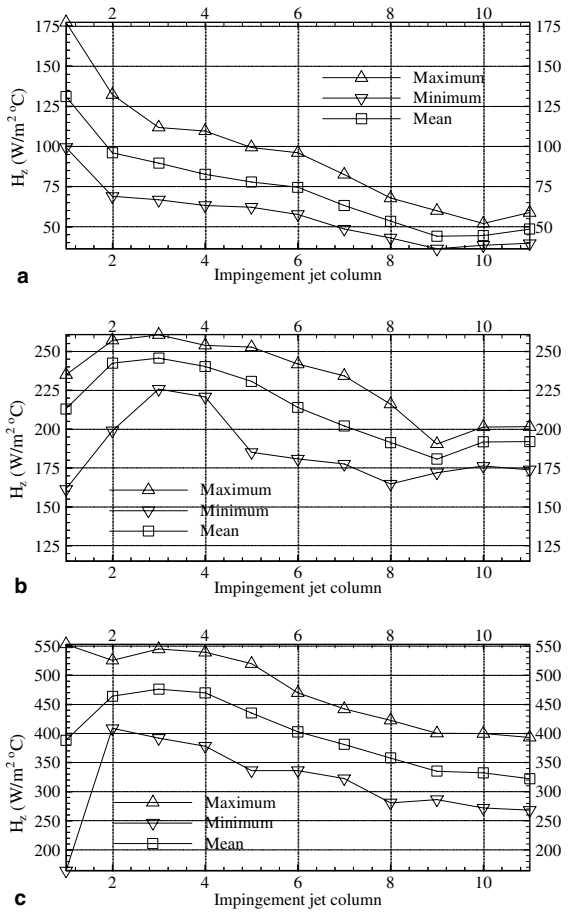


Fig. 6. Spanwise average of heat transfer coefficient distribution: (a) Case 1 at $Re = 1039$, (b) Case 2 at $Re = 3026$, and (c) Case 3 at $Re = 5133$.

commonly recognized to be caused by the "buffering or insulation effect" of the cross-flow. As Reynolds number increases, instead of a monotonically decreasing trend, $H_Z$ increases to a maximum value at the third column for both Cases 2 and 3 (Fig. 6(b) and (c)). This increasing trend of heat transfer in the first three columns is not a familiar phenomenon to the authors. It is hypothesized that this may be caused by jet-induced recirculation near the left wall. This recirculation can be induced by the entrainment from the jet shear layer. Since the strength of the circulation increases as the jet Reynolds number increases, this increasing trend of heat transfer in the first three columns occurs in higher Reynolds number cases. Recirculation induces local high pressure region near the first column and alters the flow distribution amongst the jet columns such that the Reynolds numbers of the first column becomes less than the average jet Reynolds number. This is supported by the flow measurements to be discussed later. This reversing trend of heat transfer characteristics in the first three columns can only be stated in a qualitatively way due to the fact that many other factors also affect jet impingement cooling performance. The Reynolds number values on which the heat transfer trend changes in this study shall not be held as the absolute criterion for other situations with different jet spacing or target distance.

Near the test section exit, a minor increase of $H_z$ occurs in both Case1 and Case 2. This might be caused by the possibility that the buffering effect of the cross-flow is relatively relieved near the proximity of the exit. This hypothesized "relief effect" diminished when the Reynolds number becomes large.

Comparison of spanwise $h$-distribution of the second, sixth, and eighth columns for each case is shown in Fig. 7. Case 3 shows much more reduction of $h$ from the sixth column to the eight column than in Case 1 and Case 2. All three cases show that the spanwise $h$-variation of the eight column is flatter than the previous columns. This feature indicates that spanwise heat transfer becomes more uniform as flow moves downstream.

### 4.5. Effects of cross-flow

The main objective of Case 4 is to investigate the effect of controlled cross-flow upon the heat transfer on the target surface. In the first three cases mentioned above, the impingement cavity is closed on the left side and open on the right side. In the impingement cavity, spent air is accumulated and grows thicker toward the exit. This growing mass of cross-flow exerts a significant impact on the heat transfer on the target surface. The heat transfer is primarily determined by the interactions between impingement flow and cross-flow, which makes the flow field and the heat transfer situation very complex and unpredictable.

In Case 4, both left and right sides of the test section (or impingement cavity) are open. The cross-flow divides in the geometric center of the test section between the sixth and seventh columns and builds up in both right and left directions. The left side immediately opens to the ambient atmosphere, whereas the right side opens to the right plenum of the test rig, as shown in Fig. 1. Therefore, the resistance to the flow is higher on the right side than on the left side. This difference in flow resistance is expected to affect the cross-flow rates. The merit of the present arrangement is to allow for comparing side-by-side the effect of different cross-flow rates on heat transfer at a fixed jet Reynolds number. It is expected that the cross-flow rate shall be more on the left test domain. The flow measurement verifies that the mass flow rate on the left side is 1.69 times than the right. Therefore, it is deduced that left-hand side has thicker cross-flow than does the right side. The present test condition is different from that conducted by Huang et al. [15]. In their study, both ends were open to the atmosphere, so the flow was symmetrically distributed.

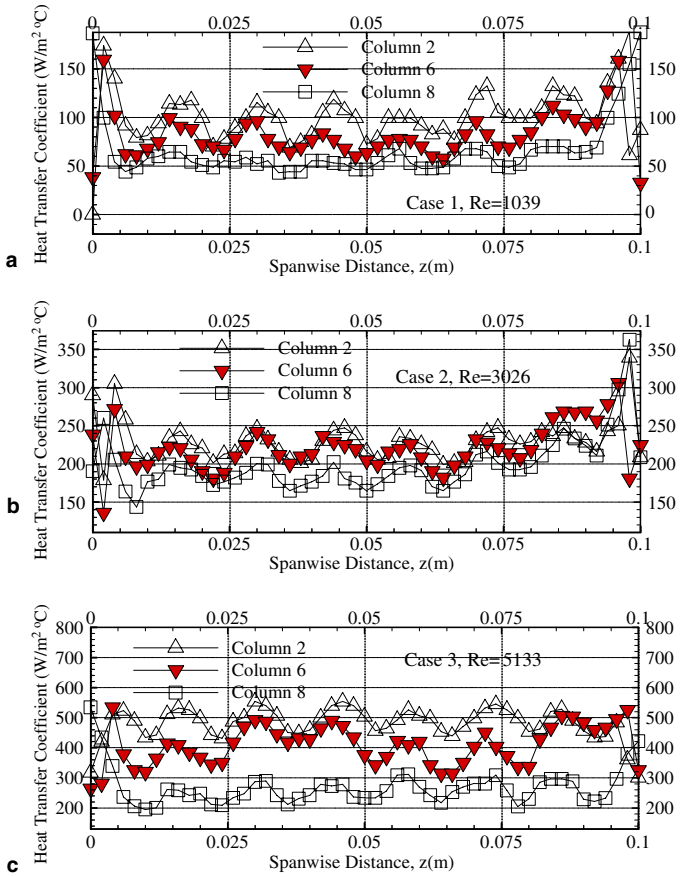


Fig. 7. Comparison of spanwise heat transfer coefficient distribution of the second, sixth, and eight columns: (a) Case 1 at $Re = 1039$, (b) Case 2 at $Re = 3026$, and (c) Case 3 at $Re = 5133$.

Fig. 8(a) presents the contour plots of $h$-distribution of Case 4, which illustrates more uniform pattern than those of Cases 1, 2, and 3. Fig. 8(b) represents the streamwise $h$-variation along a straight line through the centers of the forth row of the jet array. The overall $h$-variation tendency differs from those of Cases 1, 2, and 3. It can be clearly seen that $h$ on left-hand side decreases from the geometric center to the left-hand exit, while $h$ on the right-hand side maintains an almost constant value. This feature is also reflected in the $H_z$-distribution shown in Fig. 8(c). This result implies that increasing cross-flow by holding the jet Reynolds number constant degrades the heat transfer performance.

## 5. Nonuniformity index of surface heat transfer

As stated in the introduction, the major weakness of jet impingement cooling is its highly nonuniformly distributed heat transfer coefficient. In order to characterize this feature, two nonuniformity indices, the standard deviation of heat transfer coefficient over the whole surface ($\sigma$) and the normalized standard deviation ($\bar{\sigma} = \sigma/H$), are used to quantify the overall heat transfer performance.

Table 2 shows that Case 3 has the maximum $\sigma$-value of 107.81 W/(m$^2$ °C) among all four cases. Case 4 comes to the second place, and Case 1 has the lowest $\sigma$ of 35.24 W/(m$^2$ °C). Since different cases have different heat transfer levels, normalized standard deviation value, $\bar{\sigma}$, is more appropriate for comparing the heat transfer uniformity among these cases. Among all four cases, Case 1 has the largest $\bar{\sigma}$ value of 0.49. Case 2 has the smallest value of 0.26. The differences among these four cases are believed attributed to interactions between the jet flow and the cross-flow. The cross-flow can affect the cooling performance by two opposite manners: it can provide a buffering effect to impede cooling performance by reducing the jet flow impact on the surface, and it can also provide some minor heat transfer enhancement through increased convective cooling due to increased mass flow accumulation. These two effects

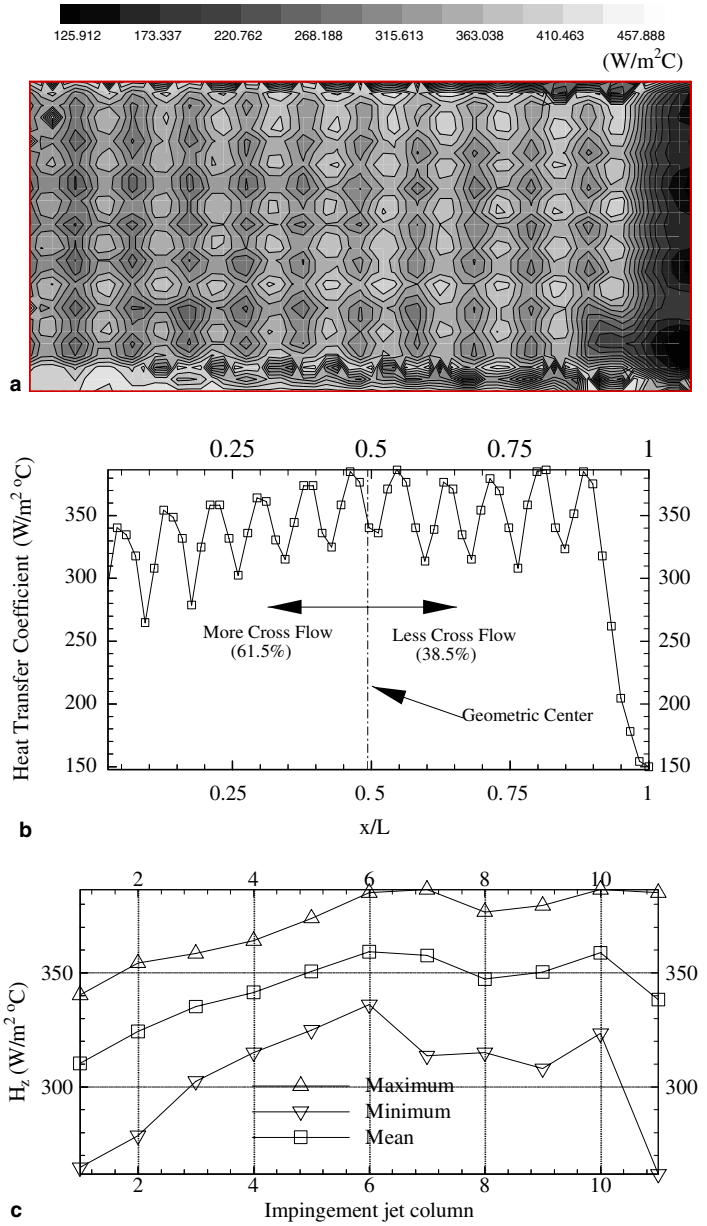


Fig. 8. Case 4 at $Re = 5175$: (a) contour plot of convective heat transfer coefficient, (b) heat transfer coefficient distribution along a straight line in the $x$-direction through the centers of the fourth row of jet array and (c) spanwise average of the heat transfer coefficient distribution.

Table 2
Comparison of uniformity of surface heat transfer performance

| Case no. | $\sigma$ (W/m °C) | $\bar{\sigma}$ |
|---|---|---|
| Case 1 | 35.24 | 0.49 |
| Case 2 | 52.20 | 0.26 |
| Case 3 | 107.81 | 0.30 |

are opposite and compete with each other. There are two other competing effects, i.e. those between the jet momentum and thickness (or mass flow rate) of the cross-flow. As the jet Reynolds number increases, the jet momentum increases and the jet strength to penetrate the cross-flow layer increases accordingly, but meanwhile, the thickness of the cross-flow also increases. In summary, overall, there are three opposite effects competing against each other, so the definite result is not

predictable. This is what has happened in the present study. As it can be seen that the $\bar{\sigma}$ value reduces as $Re$ increases from Case 1 to Case 2, but increases from Case 2 to Case 3.

The following reasoning is given to explain the above feature, although a bit trying. In Case 1, when the jet Reynolds number is low, the cross-flow is low and the effect of jet impingement is dominant. As the Reynolds number increases to 3026 in Case 2, the increase of cross-flow thickness seems to provide more buffering effect than the penetrating strength of the increased jet momentum. So the $H/Re$ value reduces from 0.0692 to 0.0674 (see Table 1), and the uniformity gets better when the $\bar{\sigma}$ value decreased from 0.49 to 0.26. However, as the jet Reynolds number continues to climb to 5133 in Case 3, the increased jet momentum seems to edge over the buffering effect of the increased cross-flow thickness. Consequently, the $H/Re$ value increases back to 0.0693, almost the same as in Case1, and the uniformity becomes worse to a value of $\bar{\sigma} = 0.3$.

The cross-flow effect is also evident from the pattern change of the contour plots, as shown in Fig. 4, from the columnar pattern in Case 1 to the horizontal pattern in Case 2 and back to the columnar pattern in Case 3. The columnar contour pattern indicates that on the surface the heat flows dominantly in horizontal direction (perpendicular to the contour lines), whereas the horizontal contour pattern indicates otherwise and that the cross-flow effects gain strength by cooling the surface more uniformly, so an almost constant $h$-value follows the cross-flow direction (i.e., horizontally in the $x$-direction). The distributions of spanwise-averaged and normalized standard deviation, $\overline{\sigma_z}$, for four cases are shown in Fig. 9. The maximum $\overline{\sigma_z}$ occurs at different column locations for different cases. The maximum $\overline{\sigma_z}$ occurs at the first column in Case 1, at the last column (exit) in Case 2 and Case 4, and at the middle column (column 6) in Case 3. It is interesting to note that Case 3 and Case 4 show a roughly symmetrical pattern. For Case 4, the nonuniformity index reaches relatively large value at both ends and is relatively lower and flat in the middle.

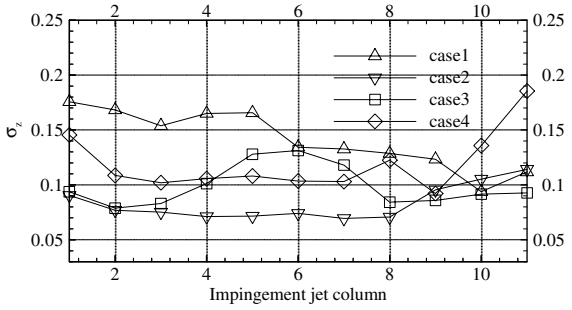


Fig. 9. Distribution of the normalized heat transfer uniformity factor in $x$-direction for all cases.

In summary, when cross-flow effect is more dominant, the nonuniformity is less, such as in Case 2. In Case 4, the cross-flow effect at the right side is small so the nonuniformity increases.

## 6. Comparison between 1-D and 3-D results

A comparison between the 3-D and 1-D results for $Re = 1039$ is shown in Fig. 10. Fig. 10(a) shows the local heat transfer coefficient value ($h$) along a horizontal straight line through the centers of the fourth row of impingement holes. The 1-D results show that the local maximum and minimum values are approximately 15–20% higher than the 3-D results. To further compare the spanwise average of the results, the whole target surface is divided into 88 sub-domains (8 rows × 11 columns) with the jet-hole location placed in the middle of each sub-domain. The measurement was made from a $240 \times 376$ array of pixels; therefore, each sub-domain contains $30 \times 34$ measurement points. Fig. 10(b) shows that the 1-D result of the spanwise average heat transfer coefficient ($H_z$) for each column is approximately 20% higher than the 3-D results. Comparison of the overall average of the heat transfer coefficient ($H$) between 1-D and 3-D results, as shown in Table 3, indicates that 1-D method overpredicts the heat transfer coefficient about 12%. This can be explained that 3-D method

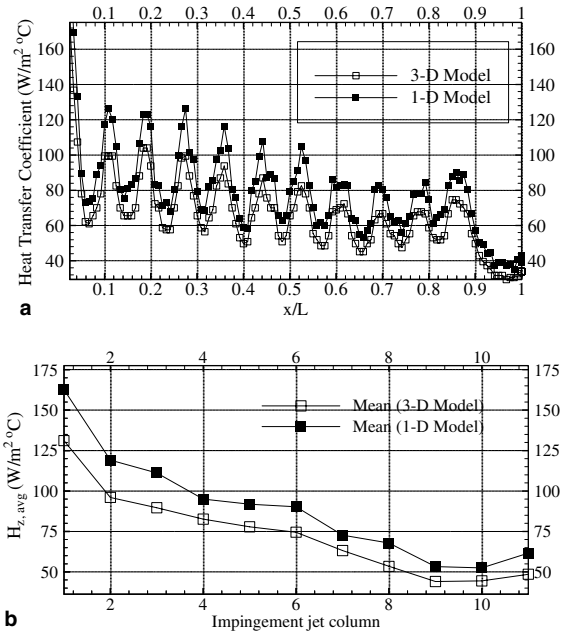


Fig. 10. Comparison between 3-D and 1-D results for $Re = 1039$: (a) local heat transfer coefficient along the center of the fourth-row of jet holes and (b) spanwise average of the heat transfer coefficients.

Table 3
Comparison between the 3-D and 1-D overall heat transfer results for one case at $Re = 1039$

| Model | $h_{min}$ (W/m$^2$ °C) | $h_{max}$ (W/m$^2$ °C) | $H$ (W/m$^2$ °C) | $H/Re$ (W/m$^2$ °C) | $Nu/Re$ |
|---|---|---|---|---|---|
| 3-D | 11.80 | 188.76 | 71.91 | 0.0692 | 0.00265 |
| 1-D | 13.28 | 210.47 | 80.83 | 0.0778 | 0.00298 |

accounts for the lateral heat flows induced by local temperature gradients, which smear out the heat transfer effect.

### 6.1. Flow field

The hot-film measurements were made for the third case with $Re = 5133$. The flow field of the present study is highly three-dimensional. The results of 2-D measurements of a highly 3-D flow field, as presented below, require cautious and careful interpretation.

### 6.2. U, V-velocity components distribution

Fig. 11 presents distributions of the $U$- and $V$-velocity components along the centerline on the measurement Plane I, which is closer to the jet issuing holes than Plane II. It should be noted that the hot-film sensors used in the present study could not detect the flow directions. Therefore, only absolute velocity values are presented in Fig. 11. The absolute value of $V$ velocity ranged from approximately 13.8 m/s to 18.2 m/s. In the third, fourth, fifth, and sixth columns, the peaks' locations roughly coincide with the locations of the impingement holes. However, in the region of the first two column impingement holes, velocity peaks do not match the impingement hole locations denoted by open circles in Fig. 11. This is believed to be caused by recirculation flow near the closed end of the impingement cavity. Downstream (in $x$-direction) of the sixth column of holes, the peak $V$ velocity has obviously shifted in the direction of the cross-flow. A secondary velocity peaks are observed between two major peaks at several locations. This can be attributed to the interactions between two columns of impingement jets. The overall trend of $V$-component of velocity increased downstream in Fig. 11(a). This implied that the jet flow rate is not uniform across the board and has a lower rate near the closed end ($x/D < 2$), which might also contribute to lower heat transfer coefficient in addition to the previous stated reason of recirculation flow.

Fig. 11(b) presents the absolute $U$-velocity component distribution along the centerline on measurement Plane I. The global distribution of $U$ velocity shows an increasing trend in the cross-flow direction with large variations occurring in the middle region of the impingement cavity.

Fig. 12 presents the $U$- and $V$-velocity component distributions along the centerline on measurement Plane

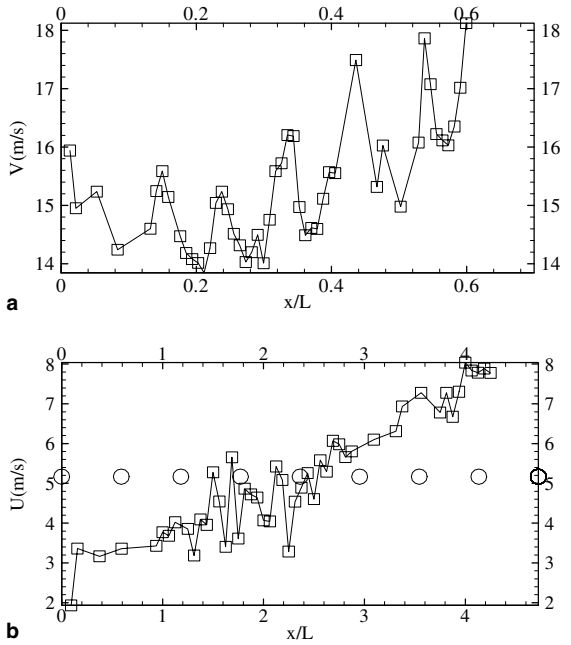


Fig. 11. Distribution of two velocity components on Plane I for Case 3 at $Re = 5133$: (a) absolute $V$-component and (b) absolute $U$-component.

II, which is near the impingement target surface. The patterns of these two figures are very similar to those of Plane I in Fig. 11. However, several differences are noticed. First, the velocity range of $V$ in Fig. 12(a) is much less than that in Fig. 11(a). This is expected because the jet velocity decays as it travels toward the target surface, and furthermore, it was retarded by the cross-flow. The $V$-velocity range on the measurement Plane II is from 5.6 m/s to 12 m/s, with the lowest velocity occurring near the third column. The maximum value and minimum value of Plane II is over 30–50% less than those of the Plane I. Secondly, the $V$-component peaks are swept downstream and occur between the jet holes.

Fig. 13 presents the average turbulence intensity distributions including both $u'$ and $v'$ along the centerline on Planes I and II, respectively. Large fluctuations of the turbulence values up to 30% are present on both planes. There is no clear correlation between the turbulence peaks and the jet holes in Fig. 13. Typically in the first five columns, the turbulence peaks occur coincidentally with

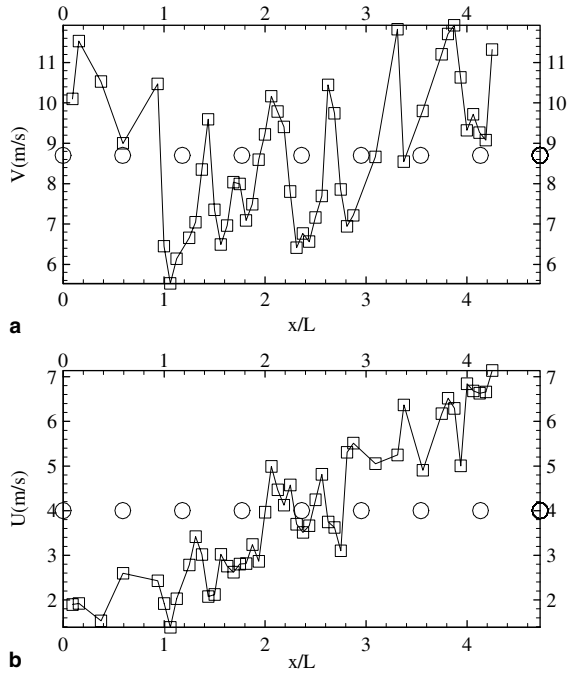


Fig. 12. Distribution of two velocity components on Plane II for Case 3 at $Re = 5133$: (a) absolute $V$-component and (b) absolute $U$-component.

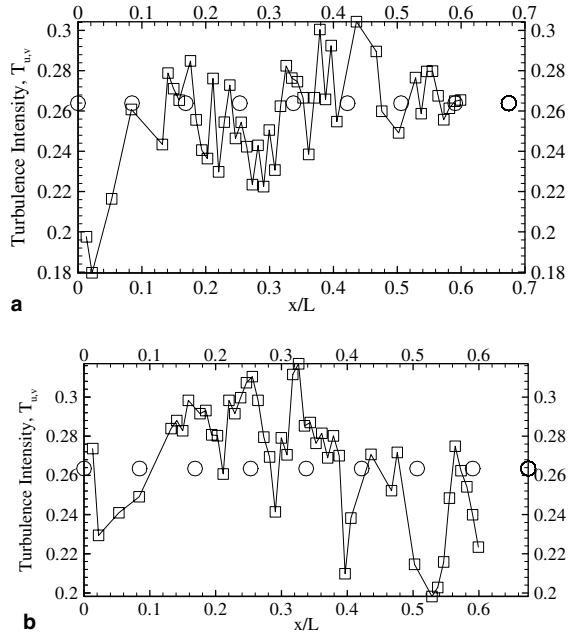


Fig. 13. Distribution of turbulence intensity for Case 3 at $Re = 5133$: (a) on Plane I and (b) on Plane II.

the jet-hole locations; but downstream of the fifth column, the turbulence peaks occur away from the jet column locations.

## 7. Conclusions

A transient liquid crystal method using hue angle and a 3-D inverse transient conduction scheme was employed to study the cooling effectiveness of $8 \times 11$ arrays of confined impinging jets. Four experimental cases were conducted at low Reynolds number range ($Re < 5200$). The first three experimental cases differed in impingement jet Reynolds numbers with only one exit. The fourth experimental case was conducted to investigate the effect of controlled cross-flow on heat transfer by opening both ends of the impingement cavity and by imposing asymmetric resistance to the flow.

Results showed that the four cases differed in their maximum and minimum heat transfer values. However, for the first three cases, there was a linear relationship between overall average heat transfer coefficient (or $Nu$) and $Re$, i.e., $H = 0.0686Re$ or $Nu = 0.00304Pr^{0.42}Re$. The results showed that due to the confined end effect, the first two jet columns do not always provide the best cooling. Designers need to know this fact and carefully evaluate the database available to them. Due to the reversing trend of the local $h$-distribution as Reynolds number changes, both extrapolation and interpretation of the database need to be cautiously performed.

The surface mapping of $h$-distribution demonstrated a change from columnar pattern to a horizontal pattern and switching back to the columnar pattern as Reynolds number increased consecutively. This pattern switching is thought to be caused by the competition between jet penetration and the cross-flow buffering effect. In Case 1 and Case 3, it was hypothesized that the jet momentums were relatively stronger than cross-flow, and therefore, the jet flow could penetrate the cross-flow and generated columnar pattern of heat transfer pattern. While in Case 2, the cross-flow buffering effect was stronger than the jet flow, which produced a horizontally stretched pattern.

The velocity measurements supported the existence of circulation in the first three columns by showing low velocity distributions than those in other regions. The results of Case 4 indicate that increased cross-flow degraded the heat transfer performance but increased uniformity. There are many parameters that are not studied in this paper but will affect the impingement jet heat transfer performance such as jet temperature, jet flow density, target distance (or channel height), jet spacing, hole geometries, and hole diameters. Applying the present results to other parametric variations require cautions.

## Acknowledgement

The first two authors want to express their gratitude to the support of General Electric Research and

Development Center and its free loan of the required compressor and test devices.

## References

[1] J.N.B. Livingood, P. Hrycak, Impingement Heat Transfer from Turbulent Air Jets to Flat Plates—A Literature Survey, NASA TM X-2778, 1973.
[2] H. Martin, Heat Mass Transfer between Impingement Gas Jets and Solid SurfacesAdvances in Heat Transfer, 13, Academic Press, New York, 1977, pp. 1–60.
[3] S.J. Downs, E.H. James, Gas Impingement Heat Transfer—a Literature Survey, ASME Paper No. 87-HT-35, 1987.
[4] A.M. Humber, R. Viskanta, Comparison of convective heat transfer to perimeter and center jets in a confined, impingement array of axis-symmetric air jets, Int. J. Heat Mass Transfer 37 (1994) 3025–3030.
[5] K. Jambunathan, E. Lai, M.A. Moss, B.L. Button, A review of heat transfer data for single circular jet impingement, Int. J. Heat Fluid Flow 13 (1992) 106–115.
[6] P.G. Huang, A.S. Mujumdar, W.J. Douglas, Numerical Prediction of Fluid Flow and Heat Transfer Under a Turbulent Impinging Slot Jet with Surface Motion and Crossflow, ASME paper 84-WA/HT-33, 1984.
[7] D.E. Metzger, T. Yamashita, C.W. Jenkins, Impingement cooling of concave surfaces with lines of circular air jets, J. Eng. Power 91 (1969) 149–152.
[8] S. Galant, G. Martinez, Crossflow influence upon impingement convective heat transfer in circular arrays of jets, a general correlation, Proc. 7th Int. Heat Transfer Conf. (1982) 343–348.
[9] R.J. Goldstein, J.F. Timmers, Visualization of heat transfer from arrays of impinging jets, Int. J. Heat Mass Transfer 25 (1982) 1857–1868.
[10] L.W. Florschuetz, R.A. Berry, D.E. Metzger, Periodic streamwise variation of heat transfer coefficients for inline and staggered arrays of circular jets with crossflow of spent air, J. Heat Transfer 102 (1) (1980) 132–137.
[11] L.W. Florschuetz, C.R. Truman, D.E. Metzger, Streamwise flow and heat transfer distribution for jet impingement with crossflow, J. Heat Transfer 103 (2) (1981) 337–342.
[12] L.W. Florschuetz, D.E. Metzger, C.C. Su, Y. Isoda, H.H. Tseng, Heat transfer characteristics for jet array impingement with initial crossflow, J. Heat Transfer 106 (1) (1984) 34–41.
[13] L.W. Florschuetz, Jet Array Impingement Flow Distribution and Heat Transfer Characteristics, NASA CR 3630, 1982.
[14] J.P. Bruchez, R.J. Goldstein, Impingement cooling from a circular jet in a crossflow, Int. J. Heat Mass Transfer 13 (1975) 719–730.
[15] Y. Huang, S.V. Ekkad, J.C. Han, Detailed heat transfer distributions under an array of orthogonal impinging jets, AIAA J. Thermophys. Heat Transfer 12 (1) (1998) 73–78.
[16] K.W. Van Treuren, Z. Wang, P.T. Ireland, T.V. Jones, Detailed measurements of local heat transfer coefficient and adiabatic wall temperature beneath an array of impingement jets, J. Turbomachinery 116 (2) (1994) 369–374.
[17] J. Hwang, C. Sheng, Impingement cooling in triangular ducts using an array of side-entry wall jets, Int. J. Heat Mass Transfer 44 (2001) 1053–1063.
[18] G. Vogel, A.B.A. Graf, J. vonWolfersdorf, B. Weigand, A novel transient heater-foil technique for liquid crystal experiments on film-cooled surfaces, J. Turbomachinery 125 (2003) 529–537.
[19] A.C. Chambers, D.R.H. Gillespie, P.T. Ireland, G.M. Dailey, A novel transient liquid crystal technique to determine heat transfer coefficient distributions and adiabatic wall temperature in a three-temperature problem, J. Turbomachinery 125 (2003) 538–546.
[20] S.V. Ekkad, J.C. Han, Detailed heat transfer distributions in two-pass square channels with rib turbulators, Int. J. Heat Mass Transfer 40 (11) (1997) 2525–2537.
[21] M. Lin, T. Wang, A transient liquid crystal method using a 3-D inverse transient conduction scheme, Intl. J. Heat Mass Transfer 45 (2000) 3491–3501.
[22] D.K. Hollingsworth, A.L. Boehman, E.G. Smith, R.J. Moffat, Measurement of temperature and heat transfer coefficient distributions in a complex flow using liquid crystal thermograph and true-color image processing, J. Heat Transfer 123 (1989) 35–42.
[23] R.J. Moffat, Contributions to the theory of single-sample uncertainty analysis, J. Fluids Eng. 104 (1982) 250–260.
[24] T. Wang, T.W. Simon, Development of a special purpose test surface guided by uncertainty analysis, J. Thermophys. 3 (1) (1989) 19–26.
[25] M. Lin, Flow and Heat Transfer of Confined Impingement Jets, MS thesis, Department of Mechanical Engineering, Clemson University, 1999.
[26] D.M. Kercher, W. Tabakoff, Heat Transfer by a Square Array of Round Air Jets Impinging Perpendicular to a Flat Surface Including the Effect of Spent Air, ASME paper 69-GT-4, March 1969.
[27] G.C. Huang, Investigation of heat transfer coefficients for air flow through round jets impinging normal to a heat transfer surface, ASME J. Heat Transfer 85 (1963) 237–243.